Soft Matter

Membrane-Mediated Dimerization of Spherocylindrical Nanoparticles

Journal:	*Soft Matter*
Manuscript ID	SM-ART-12-2022-001574.R1
Article Type:	Paper
Date Submitted by the Author:	12-Jan-2023
Complete List of Authors:	Sharma, Abash; The University of Memphis, Physics and Material Science Zhu, Yu; The University of Memphis, Physics and Materials Science Spangler, Eric; The University of Memphis, Physics and Materials Science Carrillo, Jan Michael; Oak Ridge National Laboratory Laradji, Mohamed; The University of Memphis, Physics and Materials Science

Soft Matter

ARTICLE TYPE

Cite this: DOI: 00.0000/xxxxxxxxxx

Membrane-Mediated Dimerization of Spherocylindrical Nanoparticles†

Abash Sharma,[a] Yu Zhu,[a] Eric Spangler,[a] Jan-Michael Y. Carrillo[b] and Mohamed Laradji[a*]

Received Date
Accepted Date

DOI: 00.0000/xxxxxxxxxx

We present a numerical investigation of the modes of adhesion and endocytosis of two spherocylindrical nanoparticles (SCNPs) on planar and tensionless lipid membranes, using systematic molecular dynamics simulations of an implicit-solvent model, with varying values of the SCNPs' adhesion strength and dimensions. We found that at weak values of the adhesion energy per unit of area, ξ, the SCNPs are monomeric and adhere to the membrane in the parallel mode. As ξ is slightly increased, the SCNPs dimerize into wedged dimers, with an obtuse angle between their major axes that decreases with increasing ξ. However, as ξ is further increased, we found that the final adhesion state of the two SCNPs is strongly affected by the initial distance, d_0, between their centers of mass, upon their adhesion. Namely, the SCNPs dimerize into wedged dimers, with an acute angle between their major axes, if d_0 is relatively small. However, for relatively high d_0, they adhere individually to the membrane in the monomeric normal mode. For even higher values of ξ and small values of d_0, the SCNPs cluster into tubular dimers. However, they remain monomeric if d_0 is high. Finally, the SCNPs endocytose either as a tubular dimer, if d_0 is low or as monomers for large d_0, with the onset value of ξ of dimeric endocytosis being lower than that of monomeric endocytosis. Dimeric endocytosis requires that the SCNPs adhere simultaneously at nearby locations.

1 Introduction

Owing to their unique properties, stemming from their high area-to-volume ratio, nanomaterials have a wide range of promising applications including data storage[1], light harvesting[2], nonlinear optics[3], catalysis[4], drug delivery[5], biosensing[6] and food formulation[7]. In many biomedical applications, nanoparticles (NPs) come in direct contact with living cells. Since the plasma membrane is the point of entry of all living cells, the understanding of the interaction between NPs and lipid membranes is crucial for the development of safe and effective nanomaterials for biomedical applications. This understanding can also be leveraged for the use of lipid membranes as an alternative tool for bottom-up fabrication of ordered nanostructures[8].

Competition between the adhesive energy, of the NPs on a lipid membrane, and the curvature energy of the membrane, due to its local deformation to conform to the NPs surfaces, leads the membrane to partially or fully wrap the NPs[9–17]. These deformations, which extend over length scales that are longer than the NPs dimensions, lead to an interesting membrane curvature-mediated interaction between the NPs, and can result in their aggregation. Studies of membrane-mediated interactions between two spherical NPs show four modes of adhesion, depending on their adhesion energy per unit of area, ξ[17–19]. For low values of ξ, spherical NPs are weakly wrapped by the membrane, and as a result they are highly diffusive, and their positions are uncorrelated [20]. For intermediate values of ξ, two NPs dimerize into an in-plane dimer. At higher values of ξ, the NPs dimerize into an out-plane dimer (tube). Finally, the two NPs are endocytosed at even higher values of ξ. In the case of many spherical NPs, membrane curvature-mediated many-body effects are important and lead to their aggregation into in-plane or out-of-plane linear chains[19,21,22] as well as long-lived transient states, including out-of-plane bitube and ring aggregates[22].

Recent advances in nanomaterials synthesis methods have led to engineering anisotropic NPs with an ever-increasing number of geometries, dimensions and surface properties. Particularly interesting anisotropic NPs are gold (Au) nanorods, which are endowed with optical and photothermal properties that are highly dependent on their aspect ratio[23]. Another advantage of nanorods is that, due to their stronger cross-stream drift during flow, their circulation times in capillaries are longer than those of spherical NPs[24]. A recent study showed that tracking of nanorods, with sidewise adhesion to lipid membranes, can be used to probe the mechanical properties of membranes, including

[a] Department of Physics and Materials Science, The University of Memphis, Memphis, TN 38152, USA
[b] Center for Nanophase Materials Sciences, Oak Ridge National Laboratory, Oak Ridge, TN 37831, USA
* mlaradji@memphis.edu

† Electronic Supplementary Information (ESI) available. See DOI: 10.1039/cXsm00000x/

their bending modulus and surface tension[25]. In another study, it was shown that magnetic nanorods adhering to a lipid membrane and in an oscillating magnetic field can lead to an increased local fluidization of the membrane and to its lysis[26].

Conflicting experimental results have been reported on the effect of nanorods aspect ratio $\rho = l/D$, where l and D are the length and diameter of the nanorod, respectively, on their cellular uptake[27–32]. For example, Qui *et al.* showed that the rate of uptake of Au nanorods, by HeLa and human breast adenocarcinoma cells, decreases with increasing ρ[30]. In contrast, DeBrosse *et al.* showed that the internalization of Au nanorods by keratinocyte cells increases with ρ[31]. The discrepancies between these experimental results underscores the difficulty in transferring our understanding of the interaction between NPs and living cells to that between NPs and simple lipid membranes. This is due to the fact that the internalization of NPs by cells is typically an active process that is mediated by various types of proteins which may be different for different cell types[33]. Furthermore, even in the case of passive internalization, since the plasma membrane is apposed on the cytoplasmic side to the actin cortex, which renormalizes its elastic properties[34], the adhesion of NPs to the plasma membrane should be affected by the actin cortex. The internalization process of NPs is further complicated by the fact that their typical size is of the same order of the mesh size of the actin cortex, which is about 100 nm[35]. Moreover, cooperative effects are expected to play a role on the modes of adhesion and internalization of NPs including nanorods.

A more detailed understanding of the interaction of nanorods with lipid membranes has been mainly extracted from computer simulations, which thus far have only been carried in the context of a single particle adhering to a planar membrane[36–41]. These studies demonstrate that the details of the geometry of the nanorods play a major role on their adhesion mode and the process of their internalization process. Namely, for low values of ξ, an adhering nanorod lies mainly parallel to the membrane. However, as ξ is increased, the nanorod adhesion mode undergoes a first order transition to the normal mode, in which it is in a tubular pit that is mainly perpendicular to the membrane[38,41]. The value of ξ at the transition from the parallel to the normal mode decreases with increasing D or ρ[41]. The nanorod undergoes spontaneous endocytosis at adhesion strengths beyond a threshold value ξ^*, which decreases with D but is independent of ρ[41].

Membrane-mediated interaction between nanorods was investigated analytically in the asymptotic limit of NPs with infinitely long aspect ratio[42,43]. These calculations therefore consider the case where the long axes of the NPs are parallel and can only account for the side-wise adhesion mode of the NPs. However, our understanding of the interaction between nanorods with finite aspect ratio is lacking. The aim of the present study is to investigate the adhesion modes of two nanorods on lipid membranes, their modes of dimerization and their spontaneous endocytosis. Specifically, we investigate membrane-mediated interactions between spherocylindrical nanoparticles (SCNPs) through molecular dynamics (MD) simulations of a coarse-grained model with implicit solvent[44,45]. The study is performed systematically with varying values of the adhesion strength and geometric details of the SCNP. To determine the relative stability of the different modes of adhesion, free energies are calculated using the weighted histogram analysis method[46].

2 Model and Numerical Approach

The present work is based on a mesoscale implicit-solvent model for self-assembled lipid bilayers[15,44], in which, a lipid molecule is coarse-grained into a short semi-flexible chain that is composed of one hydrophilic head (h) bead and two hydrophobic tail beads (t). The potential energy of the lipid bilayer has three contributions, and is given by,

$$U(\{\mathbf{r}_i\}) = \sum_{i,j} U_0^{\alpha_i\alpha_j}(r_{ij}) + \sum_{\langle i,j\rangle} U_{\text{bond}}^{\alpha_i\alpha_j}(r_{ij}) + \sum_{\langle i,j,k\rangle} U_{\text{bend}}^{\alpha_i\alpha_j\alpha_k}(\mathbf{r}_i,\mathbf{r}_j,\mathbf{r}_k), \quad (1)$$

where $\mathbf{r}_i$ is the coordinate of bead i, $r_{ij} = \mathbf{r}_i - \mathbf{r}_j$, and α_i ($= h$ or t) represents the type of bead i. The second summation in Eq. (1) is over bonded pairs with the lipid chains, and the third summation is over the triplets of beads constituting each lipid chain. The first term in Eq. (1) is a soft two-body potential, between beads of types α and β. This interaction is given by Eq. (A1) (ESI†). Due to the absence of explicit solvent in this model, the self-assembly of the lipid chains into bilayers is achieved through a short-range attractive interaction between the t-beads. Otherwise, h-h and h-t interactions are repulsive[15].

In Eq. (1), $U_{\text{bond}}^{\alpha\beta}$ is a harmonic potential which ensures that beads within a chain are connected, and is given by

$$U_{\text{bond}}^{\alpha\beta}(r) = \frac{k_{\text{bond}}^{\alpha\beta}}{2}\left(r - a_{\alpha\beta}\right)^2, \quad (2)$$

where $k_{\text{bond}}^{\alpha\beta}$ is the bond stiffness coefficient. Finally, $U_{\text{bend}}^{\alpha\beta\gamma}$ in Eq. (1) is a three body potential that provides bending stiffness to the lipid chains, and is given by

$$U_{\text{bend}}^{\alpha\beta\gamma}\left(\mathbf{r}_i,\mathbf{r}_j,\mathbf{r}_k\right) = \frac{k_{\text{bend}}^{\alpha\beta\gamma}}{2}\left(\cos\varphi_0^{\alpha\beta\gamma} - \frac{\mathbf{r}_{ij}\cdot\mathbf{r}_{kj}}{r_{ij}r_{kj}}\right)^2, \quad (3)$$

where $k_{\text{bend}}^{\alpha\beta\gamma}$ is the bending stiffness coefficient, and $\varphi_0^{\alpha\beta\gamma}$ is the preferred splay angle of the lipid chain taken to be 180°.

A spherocylindrical NP, of diameter D and length $l = \rho D$, where ρ is its aspect ratio, is constructed as a fairly rigid triangulated mesh following the details provided in Section SII (ESI†). We recently used this NPs model to investigate the adhesion modes of a single SCNP on planar membranes[41] and the adhesion modes of Janus spherical NPs on lipid vesicles[47]. The advantage of this model lies on the fact that the NPs are hollow, which leads to a significant reduction in the number of degrees of freedom associated with the NPs as opposed to models in which NPs are constructed from a three-dimensional arrangement of beads in some lattice structure[15,36]. This allows for simulations of relatively large and/or many NPs. Here, every n-bead of the SCNP is connected to its nearest neighbors by the harmonic potential given by Eq. (2), with a bond stiffness k_{bond}^{nn} and a preferred bond

length a_{nn}. Since the SCNP is hollow, the two-body interaction is not sufficient to provide a rigid structure of the SCNP. This problem is mitigated by introducing an additional bead, c, at the center of mass of the SCNP, that is connected to all n-beads by a harmonic bond given by Eq. (2), with a bond stiffness $k_{\rm bond}^{cn}$ and a bond length determined by the initial configuration of the SCNP.

Short-range attractive interaction between the n-beads of the SCNP and lipid head beads is ensured using $U_{\rm min}^{nh} < 0$. To prevent partial insertion of the NP in the hydrophobic core of the lipid bilayer, $U_{min}^{nt} = 0$. Beads belonging to different SCNPs (n_1 and n_2) interact with each other via the same two-body potential $U_0^{\alpha_i\alpha_j}$. Since we are interested in examining the effective interaction between two SCNPs that is fully induced by the lipid membrane, we use a two-body interaction $U_0^{n_1n_2}$ that is fully repulsive ($U_{\rm min}^{n_1n_2} = 0$) to prevent SCNPs from aggregating in the solvent. The parameters of the NP model can be tuned to affect the rigidity and the roughness of a SCNP surface.

The specific values of the model interaction parameters used in the simulations are given by,

$$\begin{aligned}
U_{\rm max}^{hh} &= U_{\rm max}^{ht} = 100\varepsilon,\\
U_{\rm max}^{tt} &= 200\varepsilon,\\
U_{\rm min}^{hh} &= U_{\rm min}^{ht} = 0,\\
U_{\rm min}^{tt} &= -6\varepsilon,\\
U_{\rm max}^{n_1h} &= U_{\rm max}^{n_1t} = 200\varepsilon,\\
U_{\rm max}^{n_2h} &= U_{\rm max}^{n_2t} = 200\varepsilon,\\
U_{\rm min}^{n_1h} &= U_{\rm min}^{n_2h} = -\mathscr{E},\\
U_{\rm min}^{n_1t} &= U_{\rm min}^{n_2t} = 0,\\
U_{\rm max}^{n_1n_2} &= 200\varepsilon,\\
U_{\rm min}^{n_1n_2} &= 0,\\
k_{\rm bond}^{ht} &= k_{\rm bond}^{tt} = 100\varepsilon/r_m^2,\\
k_{\rm bend}^{htt} &= 100\varepsilon,\\
\varphi_0^{htt} &= 180^o,\\
k_{\rm bond}^{n_1n_1} &= k_{\rm bond}^{n_2n_2} = 500\varepsilon/r_m^2,\\
k_{\rm bond}^{cn_1} &= k_{\rm bond}^{cn_2} = 10\varepsilon/r_m^2,\\
r_c &= 2r_m,\\
a_{ht} &= a_{tt} = 0.7r_m,\\
a_{cn_1} &= a_{cn_2} = \text{variable}.
\end{aligned} \tag{4}$$

D is varied between 10 and 20 nm, and ρ is varied between 1 and 2.5.

All beads are moved using a MD scheme in conjunction with a Langevin thermostat[48],

$$\dot{\mathbf{r}}_i(t) = \mathbf{v}_i(t), \tag{5}$$

$$m\dot{\mathbf{v}}_i(t) = -\nabla_i U - \Gamma\mathbf{v}_i(t) + \sigma\chi_i(t), \tag{6}$$

where m is the mass of a bead and Γ is a bead's friction coefficient. $\chi_i(t)$ is the random force originating from the heat bath. χ_i is a random vector generated from a uniform distribution and obeys $\langle\chi_i(t)\rangle = 0$ and $\langle\chi_i^{(\mu)}(t)\chi_j^{(\nu)}(t')\rangle = \delta_{ij}\delta_{\mu\nu}\delta(t-t')$, where μ and $\nu = x,\ y$ or z. , and is uncorrelated for different particles, different times, and different components. Γ and σ are interrelated through the fluctuation-dissipation theorem leading to $\Gamma = \sigma^2/2k_{\rm B}T$, where T is temperature and k_B is Boltzmann's constant.

The simulations are performed in the $NVT\Sigma$ ensemble, where N is the total number of beads in the system, $V = L_xL_yL_z$ is the system's volume, and Σ is the lateral tension applied on the bilayer along the xy-plane with the constraint $L_x = L_y = L$. The projected size of the bilayer is adjusted through a Monte Carlo scheme in which an attempted new linear system size along the xy-plane, $L' = L + \Lambda$, is selected, with Λ being a small random perturbation in the interval $[-0.1r_m,\ 0.1r_m]$. Attempted new coordinates of all beads correspond then to $x_i' = x_iL'/L$, $y_i' = y_iL'/L$, and $z_i' = z_iL'/L$. The attempted change is then accepted or rejected using the standard Metropolis criterion with the Hamiltonian $H(\{\mathbf{r}_i\}, L) = U(\{\mathbf{r}_i\}) + \Sigma L^2$. All simulations are performed on tensionless membranes ($\Sigma = 0$). Typically the initial size $(L_x, L_y, L_z) = (150r_m, 150r_m, 150r_m)$. The total number of lipids in the membrane is $N_{lip} = 70688$. This corresponds to a bare lipid bilayer with an average projected area about 150 nm $\times$ 150 nm. In all simulations, the membrane is first equilibrated during about $10^3\tau$. After this equilibration, the SCNPs are brought close to the membrane.

The simulations are executed at $k_BT = 3.0\varepsilon$, with a time step $\Delta t = 0.02\tau$, where $\tau = r_m(m/\varepsilon)^{1/2}$. Eqs. (5) and (6) are integrated using the velocity-Verlet algorithm[49] with $\Gamma = \sqrt{6}m/\tau$. The bending modulus of the bare bilayer, with the interaction parameters given by Eq. (4), as extracted from the spectrum of the height fluctuations of the bilayer, is $\kappa \approx 30k_BT$[15], which is comparable to that of a DPPC bilayer in the fluid phase[50]. By comparing the thickness of this model bilayer in the fluid phase, which is about $4r_m$, with that of a typical fluid phospholipid bilayer, which is about 4 nm, we estimate $r_m \approx 1$ nm. Hence, in the remainder of this article, all lengths are expressed in nanometers, and the adhesion energy density, ξ, is expressed in k_BT/nm^2. The adhesion energy density is defined as $\xi = |U_{adh}|/A_{adh}$, where U_{adh} is the net potential energy between the NP and the membrane and A_{adh} is the area of the NP adhering to the membrane. Details of the calculation of ξ are found in Refs.[41,47] and the relationship between ξ and $\mathscr{E}$ is shown in Fig. S2 (ESI†).

3 Results

As shown by earlier studies, a single SCNP exhibits two modes of adhesion to a planar lipid membrane, depending on the values of ξ, ρ and D[38,41]. At low values of ξ, the effect of membrane

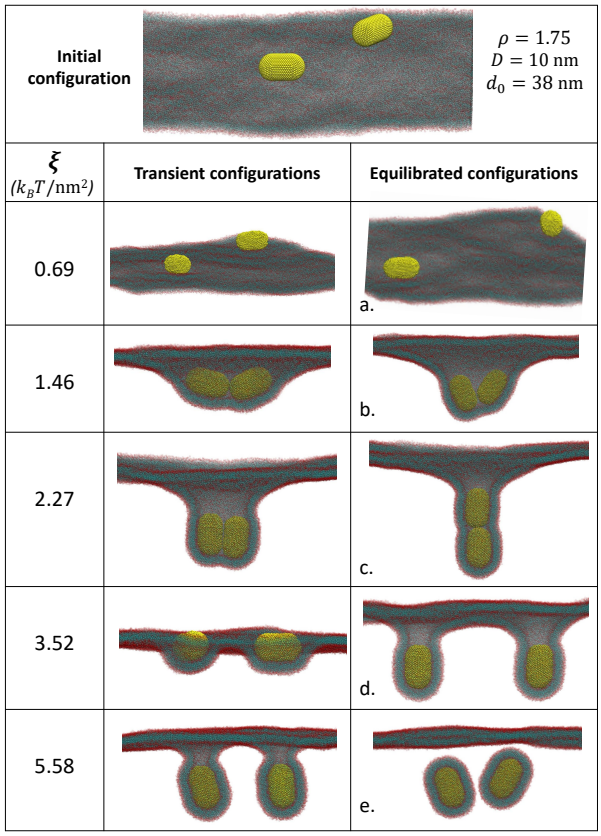

Fig. 1 Transient and equilibrium snapshots at different values of ξ in the case of SCNPs with $D = 10$ nm and $\rho = 1.75$. The SCNPs are placed initially at random orientations and at an initial distance $d_0 = 38$ nm between their centers of mass. The equilibrium state in (a) corresponds to the parallel monomeric state, in which the SCNPs lie parallel to the membrane and are fairly diffusive, without a preferred distance between them; (b) the wedged dimeric state, in which the splay angle is obtuse (acute) at relatively low (high) ξ; (c) the tubular dimeric state, in which the SCNPs are dimerized in a tube parallel to the z-axis; (d) the normal monomeric state, in which the SCNPs are parallel to the z-axis; and finally (e) the endocytosis state, in which the SCNPs are endocytosed as monomers (as shown by snapshot (e)) if they initially adhere to the membrane at large distances, or as a dimer if they initially adhere at nearby locations.

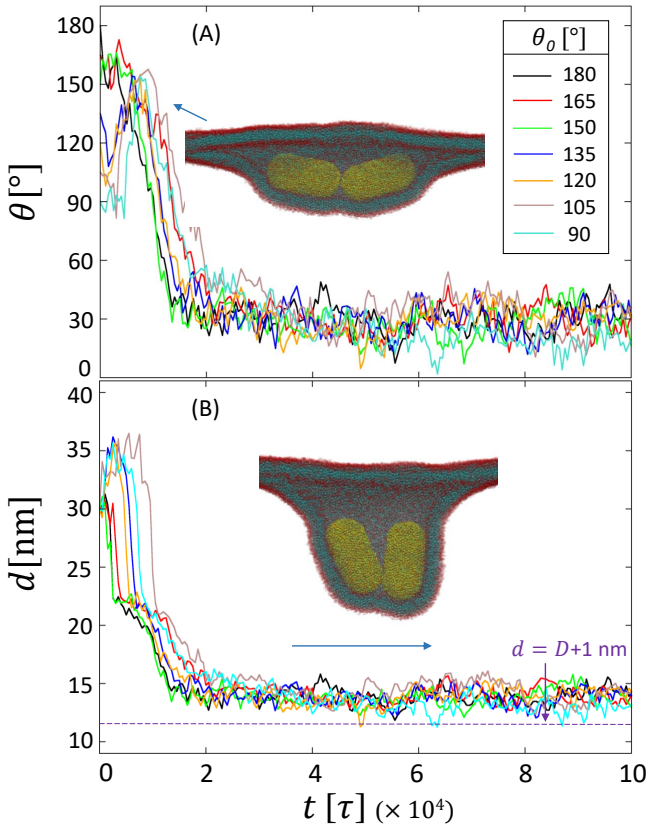

Fig. 2 (A) Angle between the SCNPs' long axes as a function of time during the dimerization process for different values of the initial angle, θ_0, between them. (B) Distance between the same SCNPs in (A). The simulations are performed in the case of two SCNPs with $D = 10$ nm and $\rho = 2.13$ at $\xi = 1.83\,k_BT$/nm^2. The initial distance between the NPs is $d_0 = 30$ nm. Inset of (A): a snapshot of the system at $t = 1.25 \times 10^4\tau$ in the case of $\theta_0 = 105°$. Inset of (B): A snapshot of the wedged dimer at equilibrium.

curvature dominates over that of adhesion, leading the SCNP to adhere sidewise (parallel mode), with its degree of wrapping that increases with ξ. Beyond some value of ξ, the effect of adhesion becomes dominant, leading the SCNP to adhere such that its long axis is perpendicular to the membrane (normal mode). The SCNP undergoes spontaneous endocytosis at even higher values of ξ.

In Fig. 1, transient and equilibrium configurations of two SCNPs, on a tensionless lipid membrane at different values of ξ, are shown for the case of $D = 10$ nm and $\rho = 1.75$. Here, the SCNPs are initially placed above an equilibrated bare membrane, such that their long axes are parallel to the xy-plane, their centers of mass are at a distance $d_0 = 38$ nm and their orientations are random. The initial distance between the long axes of the SCNPs and the average height of the head groups of the proximal leaflet of the membrane is 7.5 nm. This figure demonstrates that two SCNPs exhibit five adhesion modes on the membrane with increasing ξ. These correspond to (a) the parallel monomeric mode, in which the SCNPs lie parallel to the membrane and are highly diffusive, as demonstrated by Fig. S3 (ESI†); (b) the wedged dimeric mode, in which the SCNPs are dimerized and their long axes are at an angle $\varphi \leq 90°$ from the z-axis; (c) a tubular dimeric mode, in which the SCNPs form a tubular dimer that is mainly parallel to the z-axis; (d) a monomeric normal mode, in which the SCNPs are apart from each other and are perpendicular to the xy-plane; and (e) the endocytosis mode.

Interestingly, whether the SCNP dimerize or remain in the monomeric mode is found to not only depend on D, ρ and ξ, but also on the initial distance between them. Likewise, whether the SCNPs endocytose as monomers or as dimers also depends on the initial distance between them. This implies that kinetic effects also play an important role on the adhesion and internalization modes of SCNPs.

3.1 Effects of Initial Angle and Distance between SCNPs on their Adhesion Mode and Kinetics of Dimerization

We first inferred the effect of the initial angle, θ_0, between two SCNPs, at the onset of their adhesion to the membrane, through

a series of simulations at a value of $d_0 = 30$ nm in the case of $D = 10$ nm and $\rho = 2.13$ at $\xi = 1.83 k_B T/\text{nm}^2$. Here, θ_0 is defined as the largest angle between the long axes of the SCNPs, as indicated by Fig. S4 (ESI†). In these simulations the SCNPs are initially placed on the membrane such that their long axes are parallel to the xy-plane, and the long axis of the second SCNP intersects the long axis of the first SCNP at the center of mass of the latter. This choice of initial condition is in line with earlier studies on single SCNPs, which demonstrate that regardless of their initial orientation with respect to the membrane plane, upon their adhesion, the SCNPs quickly rotate to the parallel mode[37,41].

The time evolution of the angle $\theta(t)$, starting from θ_0, and the distance between the two SCNPs are shown in Figs. 2(A) and (B), respectively. Movies 1 and 2 (ESI†) illustrate these kinetics in the case of $\theta_0 = 180^\circ$ and 90°, respectively. Fig. 2 and Movies 1 and 2 indicate that, independent of θ_0, the SCNPs dimerise into a wedged configuration such that the equilibrium angle between them is around 30°, and the equilibrium distance between their centers of mass is around 14 nm. Fig. 2(A) indicates that the dimerization proceeds first through in-plane rotation of the SCNPs long axes such that they become temporarily almost aligned, with $\theta \gtrsim 150^\circ$. This is then followed by a rapid decrease in θ, accompanied with an invagination of the membrane by the dimer. As a result, SCNPs that are initially already aligned (i.e., cases with $\theta_0 \gtrsim 150^\circ$) dimerize faster than SCNPs with smaller values of θ_0. These results imply that the initial angle θ_0 has no effect on the final state of the SCNPs on the membrane, for the case where $d_0 \approx 30$ nm.

We now turn to the effect of the initial distance, d_0, between two SCNPs, on their final adhesion mode. To this end, we performed a series of simulations in the case of $D = 10$ nm and $\rho = 2.13$ at $\xi = 0.88$, 1.45, 1.83 and $2.24 k_B T/\text{nm}^2$, with different values of d_0 ranging between 25 and 70 nm. The SCNPs are initially placed on the membrane such that their long axes are parallel to the xy-plane and such that they are colinear. Fig. 3(A) shows that in the case of $\xi = 0.88 k_B T/\text{nm}^2$, the SCNPs generally dimerize into a wedged dimer with a large obtuse angle if $d_0 \lesssim 40$ nm, as shown by the snapshot in the same figure. This is also demonstrated by the fact that the final distance between the SCNPs, when dimerized, is very close to their length. However, for higher values of d_0, they remain in the parallel monomeric state and are highly diffusive. This figure shows, as well, that in the instance of $d_0 = 32$ nm, after spending a considerable amount of time in the monomeric mode, the SCNPs eventually dimerize at $t \approx 1.9 \times 10^5 \tau$. This indicates the existence of a relatively weak energy barrier from the monomeric state to the dimeric state at this value of ξ. However, once dimerized, the SCNPs never undimerize. This implies that the energy barrier from the dimeric state to the monomeric state at $\xi = 0.88 k_B T/\text{nm}^2$ is fairly high. Fig. 3(A) hints to a location of this energy barrier at $d^* \approx 35$ nm.

In contrast to Fig. 3(A), Fig. 3(B) shows that in the case of $\xi = 1.45 k_B T/\text{nm}^2$, the SCNPs dimerize into a wedged dimer for all considered values of d_0. The kinetics of dimerization at this value of ξ in the case of $d_0 = 55$ nm is also demonstrated by Movie 3 (ESI†). The dimer at equilibrium is a highly acute wedge in which the SCNPs are nearly parallel (see snapshots in Fig. 3(B)).

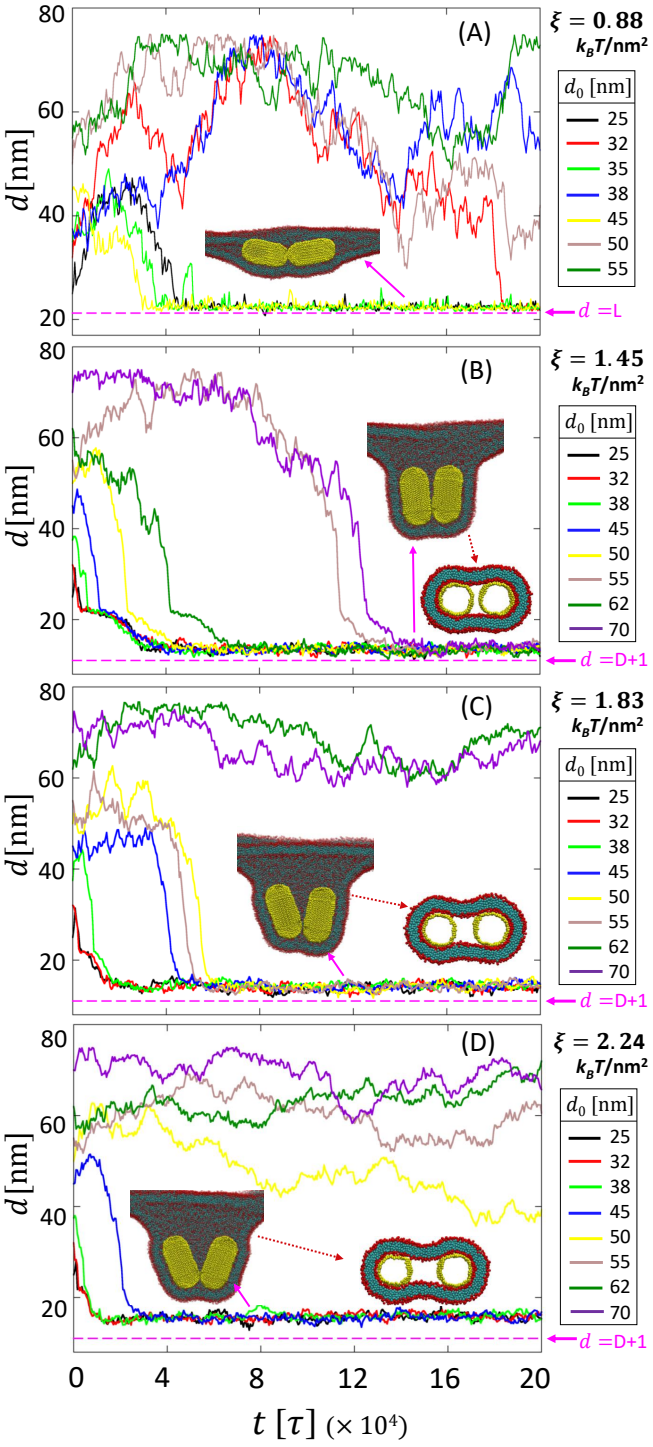

Fig. 3 Distance between the centers of mass of two SCNPs, with $D = 10$ nm and $\rho = 2.13$, vs time for different values of d_0. $\xi = 0.88 k_B T/\text{nm}^2$ for (A), $1.45 k_B T/\text{nm}^2$ for (B), $1.83 k_B T/\text{nm}^2$ for (C), and $2.24 k_B T/\text{nm}^2$ for (D). The dashed pink line in indicates in (A) indicates a distance $d = l + 1$ nm, where l is the length of the SCNPs. In (B-D), the dashed pink line indicates $d = D + 1$. The insets show the equilibrated snapshots of the systems, and cross-sections around the centers of the SCNPs.

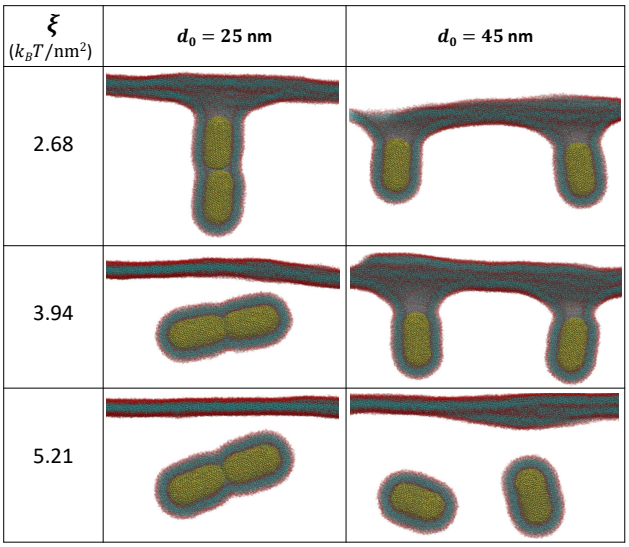

Fig. 4 Final snapshots at different values of ξ, of SCNPs with $D = 10$ nm and $\rho = 2.13$, in the cases of $d_0 = 25$ nm and $d_0 = 45$ nm.

This concurs with the fact that the distance between their centers of mass is slightly higher than D. The fact the SCNPs dimerize for all values of $d_0 \lesssim 70$ nm implies that the energy barrier between the monomeric and dimeric states at this value of ξ must be at a relatively high value of d that exceeds 70 nm. This can be explained by the fact that at $\xi = 1.45\,k_BT/\text{nm}^2$, monomeric SCNPs are in the parallel mode[41], and induce a relatively large deformation of the membrane, which must lead to relatively long-range membrane curvature-mediated attraction between them.

Figs. 3(C) and (D) show that, in the cases of $\xi = 1.83$ and $2.24\,k_BT/\text{nm}^2$, the SCNPs dimerize if $d_0 \lesssim 59$ nm and 48 nm, respectively, into acute wedged dimers. The distance between the SCNPs in this state slightly increases with ξ. This is due to the increased amount of membrane wrapping of individual SCNPs with increasing ξ, which tends to increase the angle of the wedge and pull the SCNPs apart, as demonstrated by the cross-section snapshots shown in Figs. 3(B-D). The kinetics of dimerization is illustrated by Movie 1 (ESI†) at $\xi = 1.83\,k_BT/\text{nm}^2$ and $d_0 = 30$ nm and Movie 4 (ESI†) at at $\xi = 2.24\,k_BT/\text{nm}^2$ and $d_0 = 45$ nm. For large values of d_0, the SCNPs individually flip to the normal monomeric state and do not dimerize, as also illustrated by Movie 5 (ESI†) at $\xi = 2.24\,k_BT/\text{nm}^2$ and $d_0 = 62$ nm. Therefore, for intermediate values of ξ, at which the monomeric state is the normal mode, there must exist an energy barrier between the monomeric and dimeric state, whose location decreases with increasing ξ. We note that our simulations indicate that once the SCNPs are in the normal monomeric state, they never dimerize. This hints to the presence of a fairly high energy barrier between the normal monomeric state and the dimeric states. We note that although each graph in Fig. 3 is based on a single simulation, the results shown in this figure are in fact repeatable as shown in Fig. S5 (ESI†).

The effect of initial distance on the final adhesion mode of the SCNPs was also investigated in the case where they form a tubular dimer (see snapshot (c) in Fig. 1). Fig. 4 shows that in the case of $\xi = 2.68\,k_BT/\text{nm}^2$, the SCNPs form a tubular dimer if $d_0 = 25$ nm. However, if placed at a larger distance, they individually rotate to the normal mode and do not dimerize (see right snapshot in Fig. 4 at $\xi = 2.68\,k_BT/\text{nm}^2$). Fig. 4 shows that at $\xi = 3.94\,k_BT/\text{nm}^2$, the SCNPs are endocytosed as a dimer, following their dimerization into a tubular dimer. In contrast, however, if initially placed at a large distance, they individually flip to the normal mode, but do not endocytose (see right snapshot in Fig. 4 at $\xi = 3.94\,k_BT/\text{nm}^2$). This implies that the dimerization of the SCNPs promotes their endocytosis. At $\xi = 5.21\,k_BT/\text{nm}^2$, Fig. 4 shows that the SCNPs are endocytosed as a dimer for low values of d_0 or as monomers for high values of d_0.

3.2 Kinetics of Dimerization into Wedged Dimers

We now look at the kinetics of dimerization of two SCNPs in the case of $\xi = 1.83\,k_BT/\text{nm}^2$, at an initial distance $d_0 = 45$ nm and angle $\theta_0 = 135°$. Fig. 3(C) shows that at this adhesion strength, the final state is an acute wedged dimer. The kinetics of the SCNPs dimerization is characterized by the time dependence of the distance d and angle θ between them, shown in Fig. 5(A), the angle φ between the SCNPs long axes and the z-axis, shown in Fig. 5(C), the number n of lipid head beads that are in contact with the SCNPs, shown in Fig. 5(D), and the distance h along the z-axis between the SCNPs centers of mass and the membrane's average height, shown in Fig. 5(E). Side and top views of snapshots during the dimerization process are shown in Fig. 5(A) and (B), respectively. This kinetics is also illustrated by Movie 6 (ESI†).

Fig. 5(A) shows that during the first stage (Stage I), which occurs during $0 < t \lesssim 2\times10^4\tau$, the SCNPs quickly rotate such that the angle θ between them increases to almost 180°, i.e., the SCNPs long axes become aligned while they remain mostly perpendicular to the z-axis ($\varphi \approx 90°$) as shown in Fig. 5(C). This alignment implies that the SCNPs experience an effective interaction that is mediated by the membrane curvature. Note that during this alignment stage, the distance between the SCNPs increases from 45 nm to about 50 nm, as shown by Fig. 5(A). Fig. 5(D) shows that this early stage is associated with a rapid increase in the amount of contact between the SCNPs and the membrane, which results in a rapid increase in the depth h of the NPs in the membrane (see Fig. 5(E)).

Stage II ($2\times10^4\tau \lesssim t \lesssim 6\times10^4\tau$) is characterized by an emerging attraction between the SCNPs, which leads to the decrease in the distance between their centers (see as shown by Fig. 5(A)) while they remain colinear. This is demonstrated by the high angle between them ($\theta \approx 180°$), as shown by Fig. 5(A), and by the fact that they are perpendicular to the z-axis ($\varphi \approx 90°$), as shown by Fig. 5(C). However, Fig. 5(A) shows that the SCNPs approach each other during Stage II, while their degrees of wrapping keeps increasing, as demonstrated Fig. 5(D). Eventually, the SCNPs come in contact ($d \approx 25$ nm) at the end of Stage II (see snapshots (iv) in Figs. 5(A) and (B)).

The wedged dimer forms during Stage III, which occurs during the interval $6\times10^4\tau \lesssim t \lesssim 7\times10^4\tau$. This stage is characterized by the rapid decrease in the distance d and angle θ between the SCNPs, shown in Fig. 5(A), and rapid decrease of the angles φ

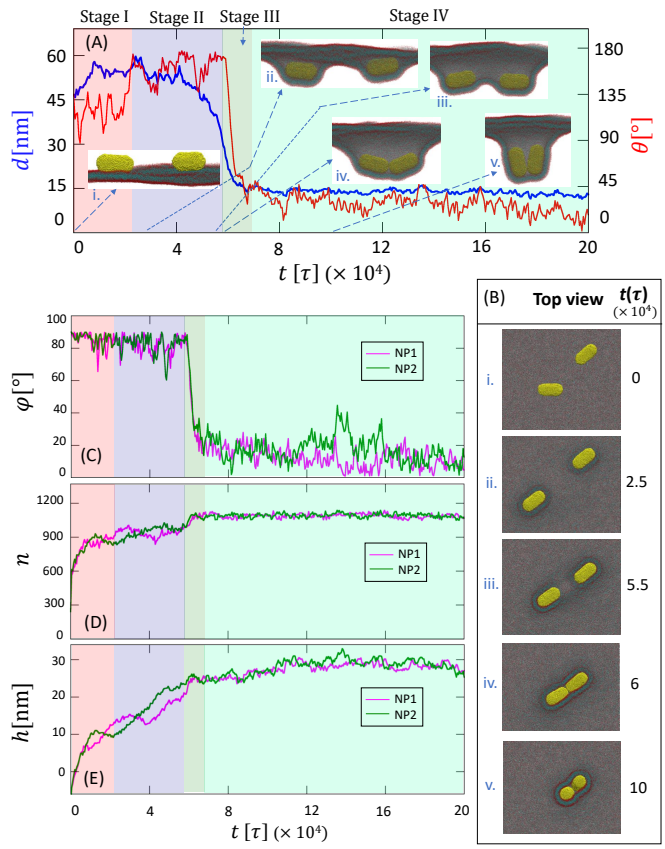

Fig. 5 Kinetics of dimerization of two SCNPs with $D = 10$ nm and $\rho = 2.13$ at $\xi = 1.83 k_B T/\text{nm}^2$. Here, the initial distance and angle between the SCNPs are $d_0 = 45$ nm and $\theta_0 = 135°$, respectively. (A) Distance and angle between the SCNPs vs time. Also shown in (A) are side-view snapshots at different times indicated by the arrows. Respective top-views of the snapshots in (A) are shown in (B). (C) Angles, φ, between the SCNPs and the z-axis (normal to the membrane). (D) Numbers of lipid head beads in contact with the SCNPs. (E) Depths of the SCNPs, along the z-axis, with respect to the average height of the membrane.

between the SCNPs long axes and z-axis. Finally, local equilibrium is reached at $t \approx 7 \times 10^4 \tau$.

In summary, Fig. 5 shows that SCNPs dimerization, into a wedged dimer, proceeds through four stages. These correspond to the alignment stage, followed by a stage during which the SCNPs are colinear and move toward each other, then followed by the third stage during which the wedged dimer forms. The wedged dimer is fully formed in the fourth stage. We note that if this numerical experiment is repeated such that $d_0 \gtrsim 60$ nm, the SCNPs individually flip to the normal monomeric mode and do not dimerize (see Fig. S6 (ESI†)).

3.3 d_0-ξ Phase Diagram

The phase diagram of the final states of two SCNPs, as a function of ξ and d_0, is shown in Fig. 6 for the case of $D = 10$ nm and $\rho = 2.13$. This phase diagram is determined from simulations based on particles adhering simultaneously to the membrane. This figure demonstrates that the final state of the SCNPs is dependent on the initial separation between them, particularly at

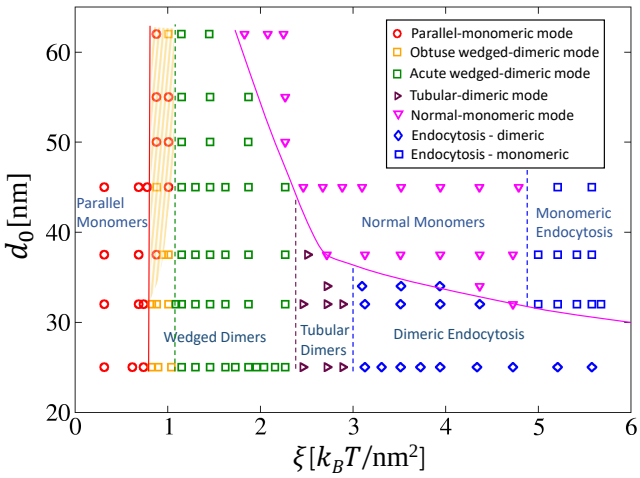

Fig. 6 Adhesion modes phase diagram in terms of the adhesion strength, ξ, and initial distance between the centers of mass of the SCNPs, in the case of $D = 10$ nm and $\rho = 2.13$. This phase diagram is extracted from the case where the SCNPs adhere simultaneously to the membrane and their long axes are initially parallel to the xy-plane. Solid lines indicate boundaries between monomeric and dimeric states. Dotted lines indicate boundaries between two monomeric states or two dimeric states.

high values of ξ. Fig. 6 shows that the SCNPs remain monomeric and in the parallel mode at low values of ξ regardless of d_0 (red squares in Fig. 6). As ξ is slightly increased, the SCNPs dimerize into the obtuse-wedged dimeric mode at low values of d_0 (orange squares). However, they remain in the monomeric parallel mode at high values of d_0, an indication of the presence of an energy barrier at a distance between them of about 35 nm, as discussed earlier, and as implicitly demonstrated by Fig. 3(A). However, since this energy barrier is weak, the SCNPs are expected to eventually dimerize. To indicate this, the region between the vertical solid red line and dashed green line, in the phase diagram of Fig. 6, is partially shaded orange.

With further increase of ξ, the SCNPs dimerize in the acute wedged dimeric mode (green symbols in Fig. 6). For relatively low values of ξ within this region of the phase diagram, the SCNPs dimerize for all considered values of d_0, as discussed in the Subsection 3.1. This is correlated with the fact that SCNPs in the monomeric state are in the parallel mode at these values of ξ. The data shown in the phase diagram is based on simulations of membranes with system size of 150×150 nm^2. Finite size effects should become important for large values of d_0. This implies that the region of the phase diagram with $1 k_B T/\text{nm}^2 \lesssim \xi \lesssim 1.8 k_B T/\text{nm}^2$ may be different for larger membranes at large values of d_0, although we found that the SCNPs dimerize even on a 300×300 nm^2 membrane at $\xi = 1.45 k_B T/\text{nm}^2$, when initially placed at $d_0 = 55$ nm, as demonstrated by Movie 7 (ESI†). This implies that finite size effects in the simulations based on 150×150 nm^2-membranes must be weak.

For values of $1.8 k_B T/\text{nm}^2 \lesssim \xi \lesssim 2.5 k_B T/\text{nm}^2$, the SCNPs dimerize only if $d_0 < d_0^*$, where d_0^* decreases with increasing ξ, as also demonstrated by Figs. 3(C) and (D). It is notable that, in this range of values of ξ, a single SCNP is in the normal monomeric

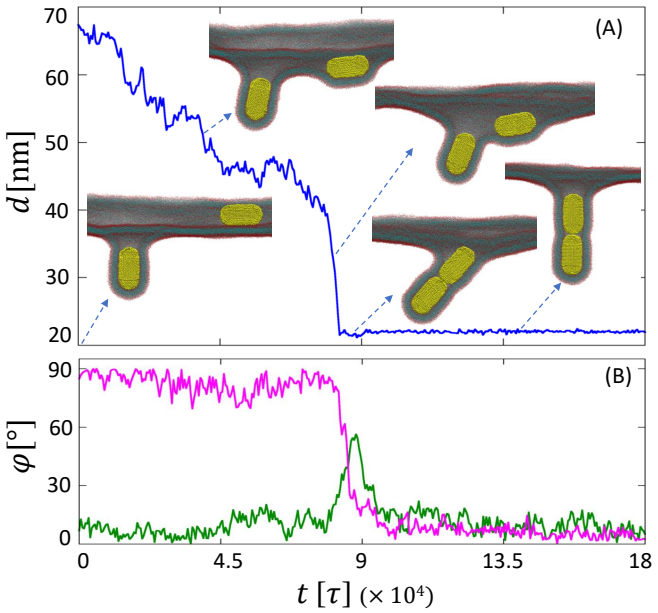

Fig. 7 Kinetics of dimerization of two SCNPs with $D = 10$ nm and $\rho = 2.13$ at $\xi = 1.63\,k_BT/\text{nm}^2$. Here, the initial distance between the centers of mass of the SCNPs is $d_0 = 70$ nm. (A) Distance between the SCNPs vs time. Also shown in (A) are side-view snapshots at different times. (B) Angles between the SCNPs and the z-axis. Snapshots in (A) correspond to configurations of the system at times indicated by the arrows.

state[41]. This reduction of d_0^* with ξ, can be understood from comparison of the time scale of dimerization τ_{dimer} and the time scale τ_{flip}, associated with the flip of a single SCNP from the parallel to the normal mode. The transition from the wedged dimeric mode to the normal monomeric mode should then occur when $\tau_{dimer} \approx \tau_{flip}$. Since τ_{dimer} increases with increasing d_0 and τ_{flip} decreases with increasing ξ[41], d_0^* should decrease with ξ.

For values of $\xi \gtrsim 2.4\,k_BT/\text{nm}^2$, two SCNPs dimerize into tubular dimers if $d_0 \lesssim 37$ nm (brown triangles in Fig. 6). However, for larger values of d_0, the SCNPs are in the normal monomeric mode. Tubular dimers endocytose at $\xi \gtrsim 3\,k_BT/\text{nm}^2$ if d_0 is small (blue diamonds). However, SCNPs in the normal monomeric mode endocytose at $\xi \gtrsim 5\,k_BT/\text{nm}^2$ (blue squares). Important conclusions drawn from this phase diagram are that the initial distance plays an important role on the final state of the SCNPs at intermediate or high values of ξ. Furthermore, their dimerisation promote their endocytosis.

3.4 Non-Simultaneous Adhesion of the SCNPs

The results presented so far are based on simulations of two SCNPs which adhere simultaneously to the membrane. In a typical experimental situation, however, NPs do not adhere simultaneously to a lipid membrane. In this subsection, we focus on the effect of non-simultaneous adhesion of SCNPs on their final adhesion mode at values of ξ, at which the first SCNP is already in the normal monomeric state. Fig. 7 shows the distance d between the two SCNPs, as well as the angles φ between their principal axes and the z-axis in the case of $D = 10$ nm and $\rho = 2.13$ at $\xi = 1.63\,k_BT/\text{nm}^2$. Here, the initial distance between the SCNPs is $d_0 = 70$ nm. This kinetics is also illustrated by Movie 8 (ESI†). This figure shows that following the adhesion of the second SCNP, the distance between their centers of mass steadily decreases while the first one remains mostly parallel to the z-axis (green curve in Fig. 7(B)) and the second one is mostly perpendicular to the z-axis (pink curve in Fig. 7(B)). During this regime, the second SCNP increasingly invaginates the membrane. Once the two SCNPs come in contact, they align to form a tubular dimer, as demonstrated by their angles ϕ becoming equal at $t \approx 9 \times 10^4 \tau$. The tubular dimer then rapidly rotates such that the angles of the SCNPs with the z-axis are almost 0. This final state is then very different from the acute wedged dimeric state which occurs in the case where the two SCNPs adhere simultaneously to the membrane at $\xi = 1.63\,k_BT/\text{nm}^2$ (see Section III.B and Fig. 5). These results are interesting in that the value of ξ of the simulation in Fig. 7, which is $1.63\,k_BT/\text{nm}^2$, is lower than that in Fig. 5 ($\xi = 1.83\,k_BT/\text{nm}^2$), at which the SCNPs form an acute wedged dimer. A question that arises then is which of the wedged dimeric state or tubular dimeric state is more stable.

3.5 Relative Stability of Different States

To determine the relative stability of the dimeric and monomeric states for a given value of ξ, we carried a large number of umbrella sampling simulations with a reaction coordinate corresponding to the distance between the SCNPs centers of mass[51]. The following bias harmonic potential energy between the SCNPs center beads was used

$$U_{\text{bias}}(d) = \frac{k_{\text{bias}}}{2}(d - d_{\text{bias}})^2, \quad (7)$$

where k_{bias} is varied between 10 ε and 100 ε, d is the distance between the SCNPs center beads and d_{bias} is the preferred distance between them. $d_{\text{bias}} = D + \lambda$, with $\lambda > r_m$. The step in d_{bias} is chosen to be sufficiently small so that there is an appreciable amount of overlap between consecutive histograms of d generated from the biased simulations. The weighted histogram analysis method (WHAM)[46] was then used to obtain the unbiased free energy of the lipid bilayer with two SCNPs as a function of the distance d. Since WHAM calculations are very costly, in general we limited our calculations to $d_{\text{bias}} < 50$ nm.

The resulting free energies for the case of two SCNPs with $D = 10$ nm and $\rho = 2.13$ at $\xi = 0.45, 0.88, 1.15, 1.30,$ and $1.83\,k_BT/\text{nm}^2$ are shown in Fig. 8. In the case of the weakest adhesion strength ($\xi = 0.45\,k_BT/\text{nm}^2$), $F(d)$ decreases monotonically with d. Therefore, the monomeric state is the only stable state in this case, in accord with the phase diagram shown in Fig. 6. However, Fig. 8 shows that, at $\xi = 0.88\,k_BT/\text{nm}^2$, the free energy has a local minimum at $d \approx 23$ nm, which corresponds to the obtuse wedged dimeric state, shown by snapshot (c) in the same figure. The free energy, at the same value of ξ, displays a local maximum at $d \approx 40$ nm, beyond which $F(d)$ decreases steadily with d, albeit at a very weak rate. The free energy should asymptotically approach a constant as d is increased. The slow decrease of the free energy with d for large values of d implies that non-dimerized SCNPs at this value of ξ can relatively easily get close to each other and overcome the small energy barrier. This explains Fig. 3(A). It is

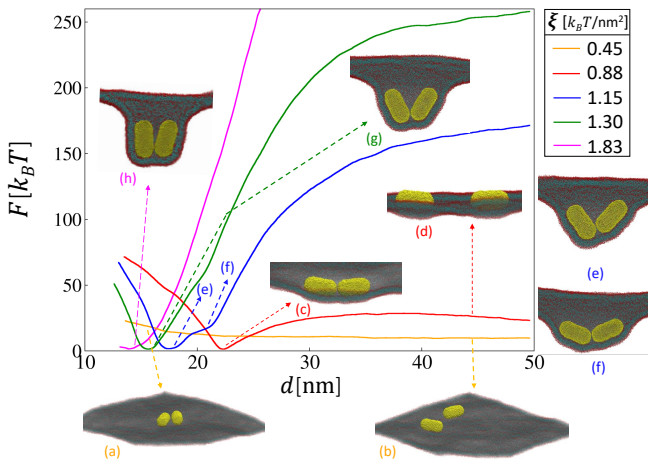

Fig. 8 Free Energy, obtained from WHAM, versus distance between the centers of mass of two SCNPs with $D = 10$ nm and $\rho = 2.13$ at different values of ξ. Snapshots (a) and (b) correspond to configurations at low ξ when the SCNPs are relatively close to and far from each other, respectively. Snapshot (c) corresponds to the minimum free energy obtuse wedged dimeric state at $\xi = 0.88\,k_BT/\text{nm}^2$. Snapshot (d) corresponds to a configuration of the undimerized SCNPs in the parallel monomeric mode at $\xi = 0.88\,k_BT/\text{nm}^2$. Snapshot (e) corresponds to a configuration of the SCNPs in the acute wedged dimeric state at $\xi = 1.15\,k_BT/\text{nm}^2$. Snapshot (f) indicates a configuration of the SCNPs in the obtuse wedged dimeric state at $\xi = 1.15\,k_BT/\text{nm}^2$. Snapshots (g) and (h) correspond to configurations of the SCNPs in the acute wedged dimeric state at $\xi = 1.30$ and $1.83\,k_BT/\text{nm}^2$, respectively.

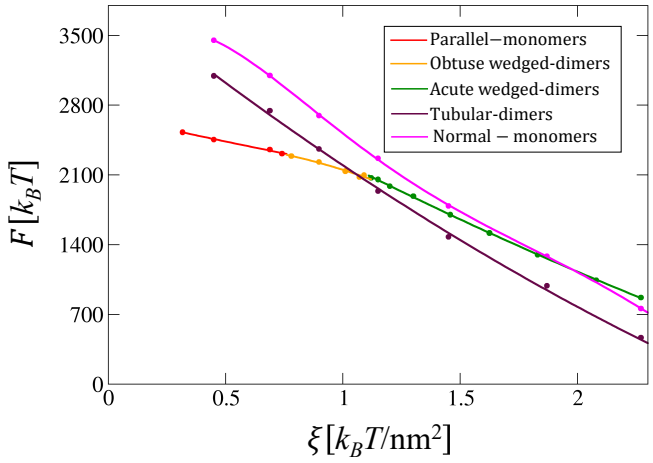

Fig. 9 Free energies of the different observed phases versus adhesion energy density, ξ for the case of $D = 10$ nm and $\rho = 2.13$.

possible that the weak decrease in the free energy at large distances for $\xi = 0.88\,k_BT/\text{nm}^2$ is due to finite size effects. If so, then for very large systems, there should not be an energy barrier from the monomeric to the dimeric state. However, we believe that this may not be the case since the largest distance of the free energy at this value of ξ is about the third of the linear system size. The energy barrier from the obtuse wedged dimeric state to the monomeric state, at $\xi = 0.88\,k_BT/\text{nm}^2$, is, in contrast, relatively high (about $25k_BT$). This implies that once dimerized, the SCNPs do not undimerize, again in agreement with Fig. 3(A).

Fig. 8 shows that the free energies, at $\xi = 1.15$, 1.30, and $1.83\,k_BT/\text{nm}^2$, exhibit clear minima corresponding to the wedged state, with configurations shown by snapshots (e), (g) and (h), respectively. We note that we were unable to detect local maxima of the free energies at higher values of d for $\xi \geq 1.15\,k_BT/\text{nm}^2$ within the range of considered values of d. However, the fact that Figs. 3 and 6 show that the SCNPs do not dimerize at high values of d_0 implies that there must be an energy barrier at some value of 50 nm $< d <$ 70 nm. Noting that we were never able to observe a dimerization of the SCNPs once they are in the normal monomeric state, the energy barrier between the wedged dimeric state and the normal monomeric state should be very high.

We were also unable to determine the relative stability of the wedged dimeric state and the tubular state, using WHAM with the distance d as a reaction coordinate, due to the lack of stable biased intermediate states between the two dimeric states. To overcome this difficulty, we used an alternative approach, which we developed earlier, for calculating the free energy based on the Helfrich Hamiltonian[52] in conjunction with a local Monge representation[22]. The free energy of the membrane with the adhering SCNPs is given by

$$F(\xi) \approx F_{\text{curv}}(\xi) + E_{\text{adh}}(\xi), \tag{8}$$

where F_{curv} is the curvature energy, which is estimated using the Helfrich Hamiltonian[52], and E_{adh} is the net adhesion energy of the SCNPs. More specifically, F_{curv} is calculated using a local Monge representation of the Helfrich Hamiltonian. Details of the Approach are found in Section SVII (ESI†). In these calculations, we do not account for the endocytosis state, since this requires adding the Gaussian bending term to the free energy and the value of the saddle splay bending modulus of our model is unknown.

The approximated free energies of the different observed adhesion modes, calculated using Eq. (8) are shown in Fig. 9 as a function of ξ in the case of $D = 10$ nm and $\rho = 2.13$. This figure shows that, excluding the endocytosis states, there are only three most stable states of two SCNPs on a lipid membrane. These correspond to the parallel monomeric state at low values of ξ, the obtuse wedged dimeric state at intermediate values of ξ, and the tubular dimeric state at high values of ξ. Of course, at even higher values of ξ, the endocytosis states become most stable. Interestingly, this phase diagram shows that the free energy of the acute wedged dimeric state is higher than that of the tubular dimeric state, regardless of ξ. From our simulations, however, the acute wedged dimeric state never spontaneously transforms to the tubular dimeric state unless $\xi \gtrsim 2.4\,k_BT/\text{nm}^2$. This implies that the energy barrier between these two states is high for $\xi \lesssim 2.4\,k_BT/\text{nm}^2$. Fig. 9 also shows that the free energy of the normal monomeric state is always higher than that of any other state, except at high values of ξ, at which the normal monomeric state becomes more stable than the tubular dimeric state. Since we never observed spontaneous transitions of the SCNPs from the normal monomeric state to other states, except the monomeric endocytosis state at $\xi \gtrsim 5\,k_BT/\text{nm}^2$, the energy barrier from the normal monomeric state to the other states (excluding the en-

docytosis state at high ξ) must be substantially higher than the thermal energy.

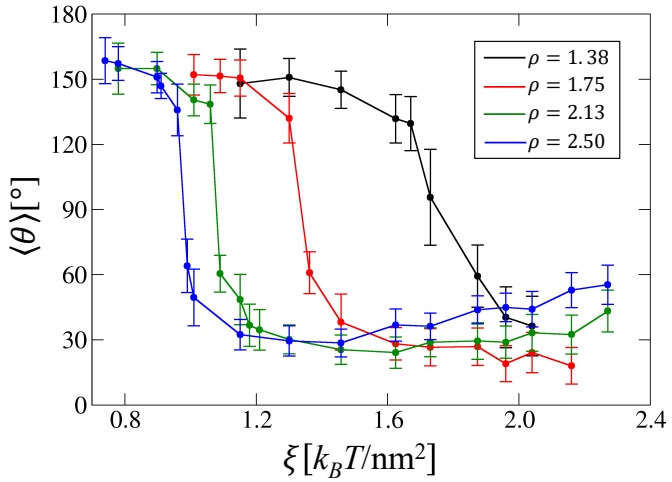

Fig. 10 Average Angle between two SCNPs as a function of ξ for the case of $D = 10$ nm at different values of aspect ratio.

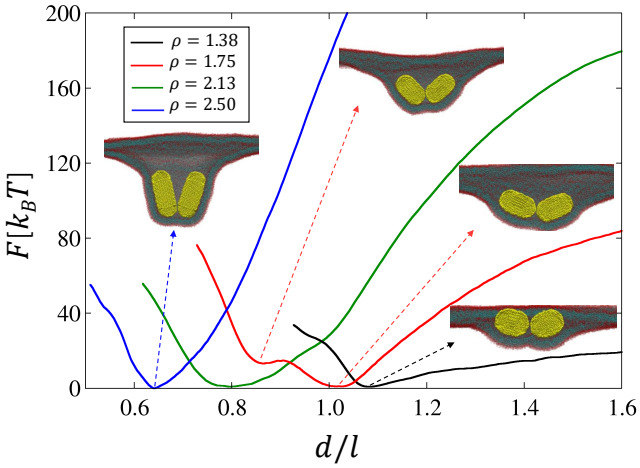

Fig. 11 Free Energy, obtained from WHAM, versus the distance between the SCNPs centers of mass, normalized by the length of the SCNPs, for different values of the aspect ratio in the case of $D = 10$ nm at $\xi = 1.3\,k_BT/\mathrm{nm}^2$.

3.6 Effect of Aspect Ratio on the Dimerization of SCNPs into the Wedged State

As stated earlier, there seems to be two wedged states in which the splay angle is either high at relatively low ξ (obtuse wedged dimeric state) or low at relatively high ξ (acute wedged dimeric state). The distinction between these two states is also hinted to by the free energy, shown in Fig. 8 for the case of $D = 10$ nm and $\rho = 2.13$ at $\xi = 1.15\,k_BT/\mathrm{nm}^2$ (blue curve), which displays an interesting shoulder to the right of the absolute minimum, whose configuration is shown by snapshot (f) in the same figure. Likewise, the free energy in the case of $\xi = 1.30\,k_BT/\mathrm{nm}^2$ also displays a shoulder, albeit weaker, to the right of the absolute minimum. These two states are of course indistinguishable for spherical or near spherical NPs[22]. To infer whether these two dimerization modes are distinct states, and determine the effect of the aspect ratio on the transition between them, we performed a series of simulations with varying values of ξ for $1.23 \leq \rho \leq 2.50$. Fig. 10 shows that, independent of the value of ρ, the average of the splay angle between the SCNPs, $\langle\theta\rangle$, decreases monotonically with ξ (except in the case of $\rho = 2.13$ and 2.50 at large values of ξ, which will be discussed below), with the sharpest decrease at some value of ξ, which decreases with increasing ρ. In the case of lowest aspect ratio ($\rho = 1.23$), the decrease is gradual. In contrast, however, the decrease is fairly abrupt for $\rho \gtrsim 1.75$. This indicates that there are actually two distinct equilibrium wedged states, namely the obtuse and acute wedged dimeric states, at relatively low and high values of ξ, and that they are likely separated by a first order transition.

An interesting feature, shown by Fig. 10, is the weak increase in $\langle\theta\rangle$ with ξ at high values of ξ within the acute wedged dimeric state, which is particularly clear for large values of ρ (e.g., blue curve). This increase is due to the increased amount of wrapping of each SCNP by the membrane as ξ is increased, which tends to separate the SCNPs from each other. This increased amount of wrapping is demonstrated by the cross-sections of the dimers shown in Figs. 3(B) to (D).

To further investigate the obtuse and acute wedged dimeric states, we conducted many umbrella sampling simulations, at $\xi = 1.3\,k_BT/\mathrm{nm}^2$, i.e close to the transition between these two states at $\rho = 1.75$, as shown by Fig. 10. The free energies, shown in Fig. 11, obtained through WHAM from these simulations, demonstrate two clear local minima for the case of $\rho = 1.75$, with the absolute minimum corresponding to the obtuse dimeric state. However, the free energy for $\rho = 1.38$ exhibits a single minimum, corresponding to the obtuse state. This agrees with Fig. 10, which shows that for this value of ρ, the SCNPs are in the obtuse wedged dimeric state at $\xi = 1.3\,k_BT/\mathrm{nm}^2$. In contrast, the free energies for $\rho = 2.13$ and 2.50, exhibit a single minimum, corresponding to the acute state, which also agree with Fig. 10. The presence of two local minima with an energy barrier at $\rho = 1.75$ indicates that the transition between the two state is likely discontinuous.

3.7 ξ-ρ and ξ-D Phase Diagrams

The results, thus far presented in this article, were mostly for the case of $D = 10$ nm and $\rho = 2.13$. The effects of D and ρ on the adhesion phase diagram of two SCNPs, and on their endocytosis, is obtained from a series of simulations at values of D ranging between 10 and 20 nm, and value of ρ ranging between 1 (spherical NPs) and 2.50. The phase diagram is obtained by initially placing the SCNPs at nearby locations on the membrane, corresponding to $d_0 = l + 5$ nm.

Fig. 12, which depicts the ξ-ρ phase diagram in the case of $D = 10$ nm, demonstrates the general sequence of phases with increasing ρ, i.e., the parallel monomeric state, the obtuse wedged dimeric state, the acute wedged dimeric state, the tubular dimeric state, and then the endocytosis state. Naturally, for $\rho = 1$ (i.e., spherical NPs), there is no difference between the two wedged

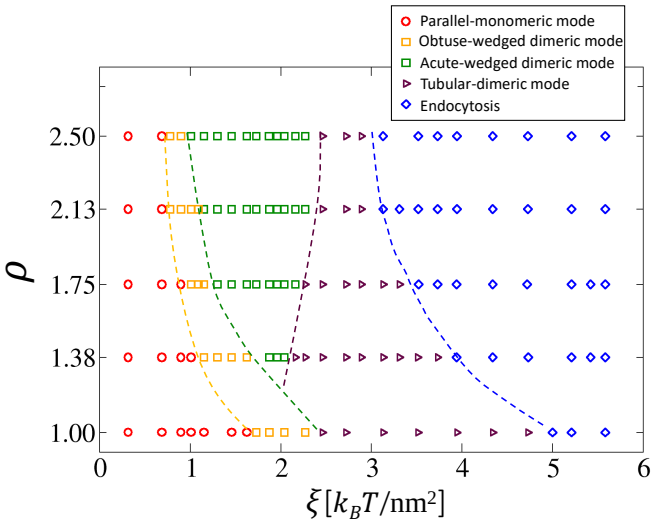

Fig. 12 $\xi - \rho$ adhesion phase diagram for 2 SCNPs in the case of $D = 10$ nm. The dotted lines are the transition lines between various phases. This phase diagram is based on MD simulations of two SCNPs with nearby initial positions, corresponding to $d_0 = l + 5$ nm.

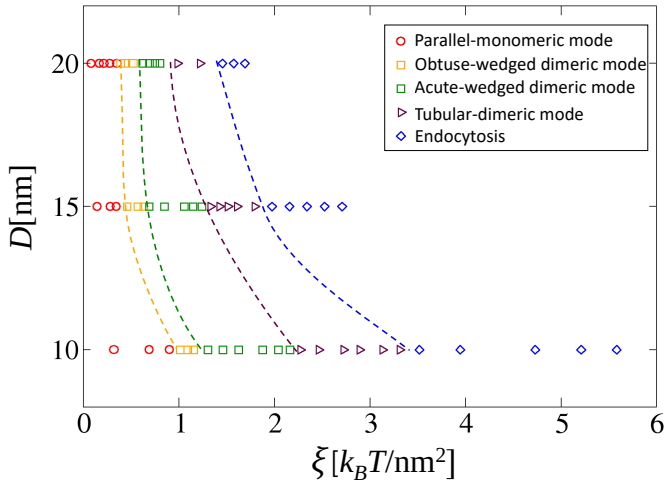

Fig. 13 $\xi - D$ adhesion phase diagram for 2 SCNPs in the case of $\rho = 1.75$. The dotted lines are the transition lines between various phases. This phase diagram is based on MD simulations of two SCNPs with nearby initial positions, corresponding to $d_0 = l + 5$ nm.

dimeric states. The acute wedged dimeric state emerges at some value of ρ lower than 1.38. Overall, this phase diagram shows that the values of ξ corresponding to the transitions between different states decrease with ρ, except the transition between the acute wedged dimeric state and the tubular dimeric state. This implies that the increase in the aspect ratio of the SCNPs, for a given diameter, promotes their dimerization, tubulation as well as endocytosis. Our results qualitatively agree with DeBrosse *et al.*, who showed that the internalization of Au nanorods by keratinocyte cells increases with increasing ρ [31].

Fig. 9 shows that the tubular dimeric state is more stable than the acute wedged dimeric state. Therefore, if we account only for the most stable states in the phase diagram, the green region, corresponding to the acute wedged dimeric state, disappears at the expense of the tubular dimeric state (maroon region).

The effect of the SCNPs diameter on their adhesion phase diagram, is shown by the ξ-D phase diagram in Fig. 13 for the case of $\rho = 1.75$. This figure shows that all transition lines between different phases decrease monotonically with ξ. This implies that increasing the SCNP's diameter, for a given aspect ratio, promotes dimerization of the NPs into wedged dimers, their dimerization into tubular dimers, and their endocytosis. As in Fig. 12, if we were to only account for the most stable states, the green region (acute wedged dimeric phase) of the phase diagram in Fig. 13 should be replaced by the maroon region (tubular dimeric phase).

3.8 Kinetic Pathway of Endocytosis of Two Spherocylindrical NPs

Finally, we focus on the kinetic pathway of the endocytosis of 2 SCNPs, in the case where they simultaneously adhere to the membrane at nearby locations. A time sequence of snapshots depicting this process is depicted in Fig. 14, for the case of 2 SCNPs with $D = 10$ nm and $\rho = 2.13$ at $\xi = 3.10 k_B T/\text{nm}^2$. This kinetics is also illustrated by Movie 9 (ESI†). The angle and distance between the SCNPs, and number of lipid head beads in contact with the SCNPs, are shown vs time in Fig. 15 for $\xi = 3.1$, 4.15 and $5.24 k_B T/\text{nm}^2$. Fig. 14 shows that, upon their adhesion, the SCNPs quickly form a wedged dimer whose splay angle decreases with time, as the SCNPs are increasingly wrapped by the membrane up to $t \approx 5500\tau$ in the case of $\xi = 3.10 k_B T/\text{nm}^2$. This is then followed by a regime up to about 15500τ, in which the SCNPs become increasingly wrapped while remaining in the wedged state, leading to slight increases in both d and θ. The upper tip of one of the two SCNPs becomes then increasingly wrapped by the membrane leading to a fast increase in d and θ. This leads the SCNPs to become increasingly colinear (see snapshots at $t = 17000$ and 18000τ) and eventual formation of a tubular dimer. The dimer is then endocytosed at $t \approx 19000\tau$. Since the effect of adhesion becomes more dominant than that of curvature with increasing ξ, the speed of this endocytosis process is increased with ξ, as shown by Fig. 15.

If the SCNPs adhere simultaneously but far from each other, they first adhere through the membrane in the parallel mode, then rotate to the normal mode [41]. The SCNPs remain attached to the membrane, in the normal monomeric mode, if $\xi \lesssim 5 k_B T/\text{nm}^2$, and endocytose individually if $\xi \gtrsim 5 k_B T/\text{nm}^2$. The same final

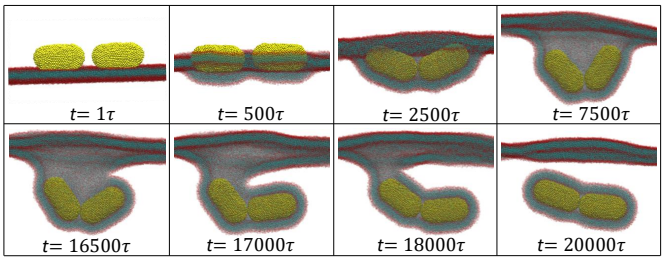

Fig. 14 Snapshot series corresponding to the case of $\xi = 3.1 k_B T/\text{nm}^2$, $\rho = 2.13$, $D = 10$ nm and $d_0 = 25$ nm.

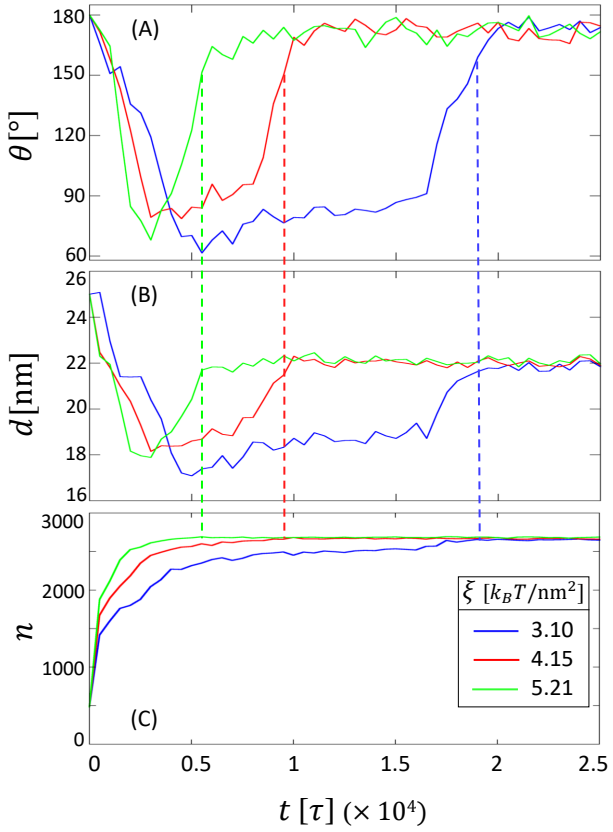

Fig. 15 (A) Angle between the SCNPs vs time for the case of $D = 10$ nm and $\rho = 2.13$ at three different values of adhesion strength. (B) Distance between the centers of SCNPs vs time for the same systems in (A). (C) Number of lipid heads beads interacting with the SCNPs vs time. The dashed lines indicate times of endocytosis.

states are also observed if the SCNPs do not adhere to the membrane simultaneously even if d_0 is very small. We note that if the two SCNPs in the dimeric tubular mode become fully normal to the membrane, their endocytosis threshold should be the same as that of a single SCNP, with same D. This is because, in this case, endocytosis is controlled by the free energy of the deformation of the neck. However, as demonstrated by Fig. 14, the SCNPs dimer does not fully become normal to the membrane. Endocytosis in fact occurs before the two SCNPs become colinear, as shown by Fig. 15. This implies that kinetic effects play a role on the endocytosis of dimerized SCNPs, i.e, endocytosis of dimerized SCNPs is not only controlled by deformation of the membrane in the neck region. This result implies that the dimerization of the SCNPs promotes their endocytosis. However, it is emphasized that endocytosis of the SCNPs as a dimer occurs only when the SCNPs adhere to the membrane simultaneously, and at close locations.

4 Summary and Conclusion

Details of the adhesion modes, dimerization and endocytosis of two spherocylindrical NPs on tensionless planar membranes are investigated using molecular dynamics simulations of a coarse-grained implicit-solvent model. The SCNPs are efficiently modeled as triangulated hollow shells[41,47]. This allows for a relatively low number of degrees of freedom associated with the SCNPs, and therefore simulations of SCNPs up to about 20 nm in diameter and 35 nm in length. The simulations were systematically performed over a range of values of the SCNPs diameter D, aspect ratio ρ, strength of the adhesion energy density ξ, and initial distance between their centers of mass d_0.

The SCNPs exhibit five different modes of adhesion, depending on the values of ξ, ρ and D. At small ξ values, they are in the monomeric-gas state and are highly diffusive. Increasing ξ leads to their aggregation into wedged dimers with an obtuse splay angle. As ξ is further increased, the obtuse wedged dimers transform into acute wedged dimers, with this transition becoming increasingly abrupt with increasing ρ. The SCNPs dimerize into tubular dimers at higher values of ξ, and are endocytosed at even higher values of ξ. Increasing the value of D or ρ promotes dimerization, tubulation and endocytosis of the SCNPs.

We also found that the final adhesion mode of the SCNPs depends strongly on the initial distance d_0 at intermediate and high values of ξ. Namely, while the SCNPs dimerize into acute wedged dimers or tubular dimers, at intermediate values of ξ, if the SCNPs adhere to the membrane at nearby locations, they remain in the monomeric normal mode if the initial distance between them is high.

Free energy calculations based on the Helfrich Hamiltonian, in conjunction with a local Monge representation[22], show that the sequence of most stable adhesion modes of two SCNPs, with increasing ξ, corresponds to the parallel monomeric mode, the obtuse wedged dimeric mode, the tubular dimeric mode, then the endocytosis mode. On the other hand, the free energy of the acute wedged dimeric mode is always higher than that of the tubular mode. Furthermore, the free energy of the normal monomeric mode is higher than those of the wedged or tubular dimeric modes. However, dimerization of the SCNPs initially in the normal monomeric mode was never observed. This implies a large energy barrier between the normal monomeric state and the wedged dimeric or tubular dimeric state. Likewise, the free energy of the monomeric normal mode is also higher than that of the other states. We note that the SCNPs never dimerize such that their long axes are parallel to each other. This implicitly implies that SCNPs experience a repulsive effective interaction when they are parallel to each other. This agrees with earlier analytical studies[42,53].

In experimental situations, NPs are not expected to adhere simultaneously to the membrane. Our simulations of non-simultaneous adhesion of two SCNPs at nearby locations, in which one of the two SCNPs is already in the normal monomeric mode show that the final state at intermediate values of ξ is the tubular dimeric mode, instead of the wedged dimeric mode. At higher values of ξ, the SCNPs do not dimerize a tubular dimer and then endocytose. Instead, both SCNPs adopt the normal monomeric mode. This implies that the two SCNPs endocytose as a dimer only when they adhere almost simultaneously and at nearby locations. Otherwise, they endocytose as monomers.

Thus far, experimental studies of SCNPs interaction with lipid membranes have been mainly conducted in the context of living cells. Our simulations agree qualitatively with DeBrosse *et al.*[31]

in that longer Au nanorods are more easily internalized by keratocytes than shorter nanorods. However, a detailed comparison between our results and existing experimental results is not possible due to the fact that the plasma membrane of living cells is apposed to the cortical cytsokeleton, which affects the elasticity of the lipid membrane, and to the presence of active effects in living cells. Experimental studies of many SCNPs interacting with simple planar lipid membranes or lipid vesicles would be very useful to validate our results.

Conflicts of interest

There are no conflicts to declare.

Acknowledgements

This work was supported by a grant from the National Science Foundation (DMR-1931837). The simulations were performed on computers of the High Performance Computing Facility at the University of Memphis. Portions of the computational aspects of this research were conducted as part of a user project at the Center for Nanophase Materials Sciences (CNMS), which is a US Department of Energy, Office of Science User Facility at Oak Ridge National Laboratory. This research used resources of the Oak Ridge Leadership Computing Facility, which is a DOE Office of Science User Facility supported under Contract DE-AC05-00OR22725. Snapshots in this article were generated using VMD version 1.9.3 [54].

Notes and references

1 S. Singamaneni, V. N. Bliznyuk, C. Binek and E. Y. Tsymbal, *J. Mater. Chem.*, 2011, **21**, 16819–16845.

2 S. Kundu and A. Patra, *Chem. Rev.*, 2017, **117**, 712–757.

3 J.-M. Lamarre, F. Billard, C. H. Kerboua, M. Lequime, S. Roorda and L. Martinu, *Opt. Comm.*, 2008, **281**, 331–340.

4 C. Yu, X. Guo, M. Shen, B. Shen, M. Muzzio, Z. Yin, Q. Li, Z. Xi, J. Li, C. T. Seto *et al.*, *Angewandte Chemie International Edition*, 2018, **57**, 451–455.

5 I. de Lázaro and D. J. Mooney, *Nat. Mater.*, 2021, **20**, 1469–1479.

6 X. Wu, C. Hao, J. Kumar, H. Kuang, N. A. Kotov, L. M. Liz-Marzán and C. Xu, *Chem. Soc. Rev.*, 2018, **47**, 4677–4696.

7 R. J. Peters, H. Bouwmeester, S. Gottardo, V. Amenta, M. Arena, P. Brandhoff, H. J. Marvin, A. Mech, F. B. Moniz, L. Q. Pesudo, H. Rauscher, R. Schoonjans, A. K. Undas, M. V. Vettori, S. Weigel and K. Aschberger, *Trends Food Sci. Technol.*, 2016, **54**, 155–164.

8 M. Wang, A. M. Mihut, E. Rieloff, A. P. Dabkowska, L. K. Månsson, J. N. Immink, E. Sparr and J. J. Crassous, *Proc. Natl. Acad. Sci. U.S.A*, 2019, **116**, 5442–5450.

9 M. Deserno and W. M. Gelbart, *The Journal of Physical Chemistry B*, 2002, **106**, 5543–5552.

10 B. J. Reynwar, G. Illya, V. A. Harmandaris, M. M. Müller, K. Kremer and M. Deserno, *Nature*, 2007, **447**, 461–464.

11 K. A. Smith, D. Jasnow and A. C. Balazs, *The Journal of chemical physics*, 2007, **127**, 08B612.

12 B. J. Reynwar and M. Deserno, *Soft Matter*, 2011, **7**, 8567–8575.

13 K. Yang and Y.-Q. Ma, *Nature nanotechnology*, 2010, **5**, 579–583.

14 T. Ruiz-Herrero, E. Velasco and M. F. Hagan, *The Journal of Physical Chemistry B*, 2012, **116**, 9595–9603.

15 E. J. Spangler, S. Upreti and M. Laradji, *J. Chem. Phys.*, 2016, **144**, 044901.

16 E. J. Spangler and M. Laradji, *The Journal of Chemical Physics*, 2020, **152**, 104902.

17 E. J. Spangler and M. Laradji, *J. Chem. Phys.*, 2021, **154**, 244902.

18 A. H. Bahrami, R. Lipowsky and T. R. Weikl, *Phys. Rev. Lett.*, 2012, **109**, 188102.

19 A. Šarić and A. Cacciuto, *Phys. Rev. Lett.*, 2012, **109**, 188101.

20 L. He, Y. Li, L. Wei, Z. Ye, H. Liu and L. Xiao, *Nanoscale*, 2019, **11**, 10080–10087.

21 A. Šarić and A. Cacciuto, *Phys. Rev. Lett.*, 2012, **108**, 118101.

22 E. J. Spangler, P. B. S. Kumar and M. Laradji, *Soft Matter*, 2018, **14**, 5019–5030.

23 Y. Hua, K. Chandra, D. H. M. Dam, G. P. Wiederrecht and T. W. Odom, *J. Phys. Chem. Lett.*, 2015, **6**, 4904–4908.

24 R. Toy, E. Hayden, C. Shoup, H. Baskaran and E. Karathanasis, *Nanotech.*, 2011, **22**, 2446–2456.

25 M. Molaei, S. K. Kandy, Z. T. Graber, T. Baumgart, R. Radhakrishnan and J. C. Crocker, *Phys. Rev. Research*, 2022, **4**, L012027.

26 I. M. Le-Deygen, K. Y. Vlasova, E. O. Kutsenok, A. D. Usvaliev, M. V. Efremova, A. O. Zhigachev, P. G. Rudakovskaya, D. Y. Golovin, S. L. Gribanovsky, E. V. Kudryashova, A. G. Majouga, Y. I. Golovin, A. V. Kabanov and N. L. Klyachko, *Nanomedicine: Nanotechnology, Biology and Medicine*, 2019, **21**, 102065.

27 B. D. Chithrani, A. A. Ghazani and W. C. Chan, *Nano lett.*, 2006, **6**, 662–668.

28 Y.-F. Huang, H.-T. Chang and W. Tan, *Analytical Chemistry*, 2008, **80**, 567–572.

29 S. E. A. Gratton, P. A. Ropp, P. D. Pohlhaus, J. C. Luft, V. J. Madden, M. E. Napier and J. M. DeSimone, *Proc. Natl. Acad. Sci. U.S.A.*, 2008, **105**, 11613–11618.

30 Y. Qiu, Y. Liu, L. Wang, L. Xu, R. Bai, Y. Ji, X. Wu, Y. Zhao, Y. Li and C. Chen, *Biomaterials*, 2010, **31**, 7606–7619.

31 M. C. DeBrosse, K. K. Comfort, E. A. Untener, D. A. Comfort and S. M. Hussain, *Mater. Sci. Eng. C*, 2013, **33**, 4094–4100.

32 P. Falagan-Lotsch, E. M. Grzincic and C. J. Murphy, *Proc. Natl. Acad. Sci. U.S.A.*, 2016, **113**, 13318–13323.

33 M. S. de Almeida, E. Susnik, B. Drasler, P. Taladriz-Blanco, A. Petri-Fink and B. Rothen-Rutishauser, *Chemical Society Reviews*, 2021, **50**, 5397–5434.

34 R. Rodríguez-García, I. López-Montero, M. Mell, G. Egea, N. S. Gov and F. Monroy, *Biophysical Journal*, 2015, **108**, 2794–2806.

35 P. Chugh and E. K. Paluch, *J. Cell Sci.*, 2018, **131**, jcs186254.

36 R. Vácha, F. J. Martinez-Veracoechea and D. Frenkel, *Nano Lett.*, 2011, **11**, 5391–5395.

37 C. Huang, Y. Zhang, H. Yuan, H. Gao and S. Zhang, *Nano lett.*, 2013, **13**, 4546–4550.

38 S. Dasgupta, T. Auth and G. Gompper, *Nano Lett.*, 2014, **14**, 687–693.

39 X. Yi and H. Gao, *Phys. Rev. E*, 2014, **89**, 062712.

40 H. Tang, H. Zhang, H. Ye and Y. Zheng, *The Journal of Physical Chemistry B*, 2018, **122**, 171–180.

41 A. Sharma, Y. Zhu, E. J. Spangler and M. Laradji, *J. Chem. Phys.*, 2022, **156**, 234901.

42 T. R. Weikl, *The European Physical Journal E*, 2003, **12**, 265–273.

43 Z. Wu and X. Yi, *Phys. Rev. E*, 2021, **104**, 034403.

44 J. D. Revalee, M. Laradji and P. Sunil Kumar, *J. Chem. Phys.*, 2008, **128**, 01B614.

45 M. Laradji, P. B. S. Kumar and E. J. Spangler, *Journal of Physics D: Applied Physics*, 2016, **49**, 293001.

46 S. Kumar, J. M. Rosenberg, D. Bouzida, R. H. Swendsen and P. A. Kollman, *J. Comp. Chem.*, 1992, **13**, 1011–1021.

47 Y. Zhu, A. Sharma, E. J. Spangler and M. Laradji, *Soft Matter*, 2022, **18**, 4689–4698.

48 G. S. Grest and K. Kremer, *Phys. Rev. A*, 1986, **33**, 3628.

49 W. C. Swope, H. C. Andersen, P. H. Berens and K. R. Wilson, *J. Chem. Phys.*, 1982, **76**, 637–649.

50 J. F. Nagle, M. S. Jablin, S. Tristram-Nagle and K. Akabori, *Chemistry and physics of lipids*, 2015, **185**, 3–10.

51 G. M. Torrie and J. P. Valleau, *Chem. Phys. Lett.*, 1974, **28**, 578–581.

52 W. Helfrich, *Z. Naturforsch., C, J. Biosci.*, 1973, **28**, 693–703.

53 M. M. Müller, M. Deserno and J. Guven, *Physical Review E*, 2007, **76**, 011921.

54 W. Humphrey, A. Dalke and K. Schulten, *J. Mol. Graph.*, 1996, **14**, 33–38.